Title
On the Nature of Field-Enhanced Water Dissociation in Bipolar Membranes

Journal
The Journal of Physical Chemistry C, 125(45)

ISSN
1932-7447

Authors
Bui, Justin C
Corpus, Kaitlin Rae M
Bell, Alexis T
et al.

Publication Date
2021-11-18

DOI
10.1021/acs.jpcc.1c08276

Peer reviewed

On the Nature of Field-Enhanced Water Dissociation in Bipolar Membranes

Justin C. Bui[1,2*], Kaitlin Rae M. Corpus[1,2], Alexis T. Bell[1,2], and Adam Z. Weber[2*]

[1] Department of Chemical and Biomolecular Engineering
University of California Berkeley
Berkeley, CA 94720, USA

[2] Liquid Sunlight Alliance
Lawrence Berkeley National Laboratory
Berkeley, CA 94720, USA

***Corresponding Authors**

email: justinbui@lbl.gov
phone: (571) 269-0395

email: azweber@lbl.gov
phone: (510) 486-6308

Abstract

Bipolar membranes (BPMs) possess the potential to optimize pH environments for electrochemical-synthesis applications when employed in reverse bias. Unfortunately, the performance of BPMs in reverse bias has long been limited by the rate of water dissociation (WD) occurring at the interface of the BPM. Herein, we develop a continuum model of the BPM that agrees with experiment, and models explicitly multiple kinetic pathways for WD in the BPM junction catalyst layer, seeking to understand and enhance WD catalyst performance. The model reveals that WD catalysts with a more highly alkaline or acidic pH at the point of zero charge (pH_{PZC}) exhibit accelerated WD kinetics, because the more acidic or alkaline pH_{PZC} catalysts possess greater surface charge, enhancing the local electric field and rate of WD. The model is then employed to explore the sensitivity of the BPM performance to various BPM physical parameters. Finally, the model is used to simulate the operation of bi-metallic WD catalysts, demonstrating that an optimal bi-metallic catalyst has an acidic pH_{PZC} catalyst matched with the cation-exchange later and an alkaline pH_{PZC} catalyst matched with the anion-exchange layer. The study provides insight into the operation of BPM WD catalysts and gives direction toward the development of next-generation WD catalysts for optimal BPM performance under water-splitting and related conditions.

Introduction

Bipolar membranes (BPMs) will be critical to the future of sustainable electrochemical synthesis due to their ability to enable stable optimized pH microenvironments at individual electrodes. This is especially intriguing for reverse-bias applications, such as CO_2 reduction and water splitting, where optimal pH conditions for each electrode can exist that also minimize CO_2 crossover.[1–6] However, BPMs have long been limited in their application due to the considerable applied potentials required to drive the water dissociation (WD) occurring at the interface of the anion-exchange layer (AEL) and cation-exchange layer (CEL) of the BPM.[4,7–10] Many prior BPMs require approximately 1 V of membrane potential to achieve 10 mA cm^{-2} of WD current density.[11–17] Further research is required to understand the nature of the issue and ameliorate it to develop BPMs that can enhance the WD current densities achievable in BPMs.

Recent studies have surmised that the key to attaining enhanced WD current densities is the development and incorporation of new interfacial WD catalysts.[18,19] Shen *et al.* achieved significant WD current density (100 mA cm^{-2} at < 1 V) using a catalyst layer (CL) with a 3D-electrospun junction.[20] They propose that the 3D-geometry of the electrospun CL had a high active surface area, enabling the achievement of improved current densities.[20] Oener *et al*. achieved current densities greater than 1 A cm^{-2} with a bi-functional, bi-metallic WD catalyst, where the point of zero charge (PZC) of each catalyst was matched to the pH of the adjacent ion-exchange layer.[19] Nonetheless, there have been few studies establishing the mechanisms of WD in BPM CLs,[11,21–23] and no theory has adequately explained the performance demonstrated by state-of-the-art WD catalysts.[18–20] Therefore, there exists a significant need to enhance the understanding of WD in order to facilitate the design of high performance WD catalysts.

Although there is still substantial disagreement regarding the nature of the WD mechanism, most theoretical studies have agreed that WD catalysis in BPM interfaces arises from enhanced dissociation kinetics resulting from the electric-field enhancements as described by the Second Wien Effect.[22,24–31] In the Second Wien Effect, molecules with well-defined dipole moments (*i.e.* water) can orient in a large electric field. This reorientation reduces the free energy of the Bjerrum dipole transition state and subsequently increases the escape rate of ions exponentially.[22,29] The electric field in a BPM interface can achieve values of up to 10^8 V m^{-1} during operation, which is sufficiently large to accelerate the rate of WD beyond the rate of recombination of hydronium and hydroxide.[9,25]

To explain field-enhanced WD in BPMs, several simplified models of catalytically enhanced WD have been developed. Our prior work developed a model of catalytically enhanced WD that simply scaled the term within the exponential of the Second Wien Effect by a "catalyst effectiveness factor" for regions where the WD catalyst was present.[23] This effectiveness factor was used as a fitting parameter to enable the matching of a coupled reaction-transport simulation to experimental BPM polarization curves operating in various electrolytes. Simulations by Yan *et al.* modeled the catalyst enhancement as a two order of magnitude increase in the rate of dissociation compared to that of recombination in the junction region of the BPM.[32] The studies by Mafé *et al.* established an analytical model for Onsager's Second Wien Effect[27,28] applied to WD at the BPM interface. Using this analytical model, coupled reaction-transport equations were solved analytically to derive expressions for the polarization curves of BPMs in forward and reverse bias.[24–26] Grew *et al.* invoked an analogy to semiconductors, modeling hydronium and hydroxide generation in the BPM interface similarly to charge carrier generation in a semiconductor pn junction.[33] Mareev *et al.* developed a continuum model that employed Mafé's

WD kinetics, solving for the transport of all ionic species within the BPM. This work enabled understanding of the local ionic concentrations and electric-field intensity at the BPM interface.[22] Craig *et al.* and Lin *et al*. developed similar continuum models that also accounted explicitly for the protonation of the WD catalyst species in the BPM junction.[11,21] These studies provided the initial understanding of the nature of charged species formation in the WD catalyst during BPM operation. However, while these models are very useful for understanding macroscale ion transport within the BPM, they fail to provide concrete recommendations for guiding the design of BPM WD catalysts.

Unfortunately, while these investigations have substantially improved the mechanistic understanding of WD in BPM junctions, they provided few concrete recommendations regarding the design of novel WD catalysts. Prior studies investigating WD catalysis through continuum simulation proposed modifications to the pK_a of the WD catalyst, which is not easily measured.[11,22,34] In Oener *et al.*'s seminal work, the authors proposed the use of the pH at the PZC (pH_{PZC}) as an alternative metric in evaluating the performance of transition-metal WD catalysts.[19] Additionally, their work demonstrated that bi-metallic WD catalysts, where the acidity or alkalinity of the pH_{PZC} is matched to the adjacent ion-exchange layer, are optimal for accelerating WD. However, the origin of the enhancements is still poorly understood; developing theory to rationalize the effect of the pH_{PZC} on the performance of a WD catalyst is necessary to properly guide the design of next-generation WD catalysts.

In this work, we present an experimentally-validated, multi-scale, continuum simulation of coupled reaction-transport in a BPM that accounts for the transport of hydroxides, hydronium, and salt-ion species, along with field enhanced WD, and the protonation and deprotonation mechanisms of the WD catalyst. In doing so, a more complete picture of the mechanism of WD in

BPM junctions is realized that elucidates the effect of the WD catalyst and the nature of field-enhanced WD at BPM interfaces. The simulation is then used to evaluate sensitivity to various BPM, AEL, CEL, and WD catalyst physical and chemical parameters and to provide recommendations for the design of next-generation materials and designs for high-performance BPMs.

Model development

The following section describes the modeling methodology, governing equations, and assumptions employed to simulate the electrochemical performance of BPMs, and to elucidate the mechanism of WD at the CEL/AEL junction. The domain modeled is a 1-D representation of that between the two reference electrodes in a standard 4-electrode measurement. In a 4-electrode cell, shown schematically in **Figure 1a**, an applied potential is measured between two reference electrodes placed near the BPM (one on either side) via Luggin capillaries.[11] This device configuration is typically used to characterize the current-voltage characteristics of the BPM because the two reference electrodes facilitate the deconvolution of the applied membrane potential required to drive WD in the BPM from the overpotentials required to drive the faradaic reactions occurring at the anode and cathode.[12,23] Numerically, the choice of domain simplifies the boundary conditions, enabling the use of Dirichlet boundary conditions for the electrostatic potential on either side of the membrane as well as for the bulk concentrations within the anolyte and catholyte.[23]

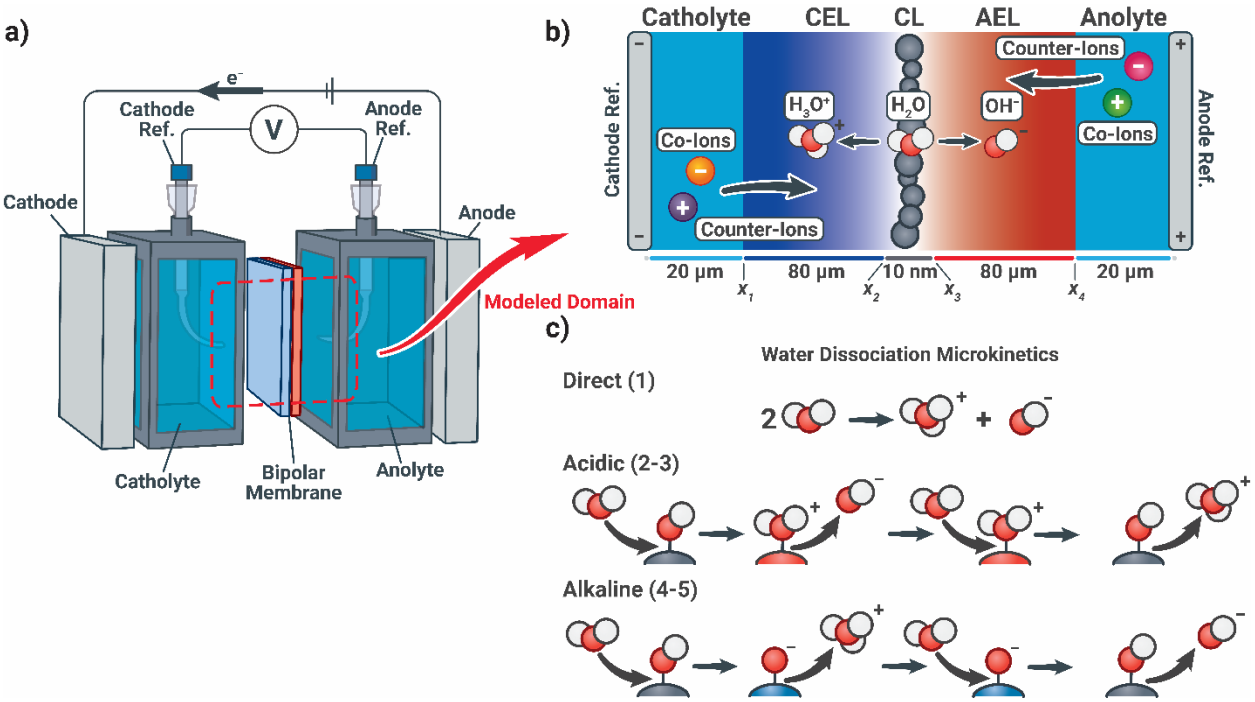

Figure 1: (a) Schematic representation of a standard 4-probe experimental set up, where the red box indicates the modeled domain. **(b)** Schematic representation of modeled domain. **(c)** Diagram of microkinetic WD pathways as implemented in the model.

The modeled domain (**Figure 1b**) is simulated in 1-dimension in the through-plane (z) direction of the 4-probe cell with a phosphate buffer electrolyte (for consistency with experiment[12]) assuming uniform concentration and potential profiles in-plane (x and y). The simulation captures physical phenomena in both the aqueous electrolyte phases and ionomer phases to represent electrochemical current-voltage relationships measured experimentally. These phenomena include the transport of all ionic species and water, homogeneous reaction kinetics that occur in the bulk electrolyte and ionomer phases, and field-enhanced WD in the CL. As depicted, the model is comprised of a cathodic reference electrode (Cathode Ref.), a 20 µm catholyte boundary layer (Catholyte), an 80 µm CEL, a 10 nm WD CL, an 80 µm AEL, a 20 µm anolyte boundary layer (Anolyte), and an anodic reference electrode (Anode Ref.). CEL and AEL thicknesses are extracted from technical specifications of the widely-used Fumatech FBM BPM.[35] The WD CL

thickness has not been measured for the Fumatech FBM, and is thus set to 10 nm for the reference case, consistent with previous simulation studies.[11,21] Regarding the choice of the 20 μm boundary layer thicknesses, because the potential drop within the boundary layer is negligible compared to that within the membrane, our prior work has shown that BPM performance is relatively insensitive to the boundary-layer thickness.[23] This insensitivity is further demonstrated in **Figure S1**. Alternatively, a simulation of a full zero-gap cell (*i.e.*, a membrane-electrode assembly) or a gas-diffusion electrode could be employed. However, these systems involve more complex multi-phase transport and computationally intensive Robin-type boundary conditions; such a model is beyond the scope of the current work, which is focused on the BPM phenomena.

Water dissociation kinetics

To model the kinetics of field enhanced WD throughout the BPM, a modified microkinetic model was developed that includes three distinct pathways for WD to occur, shown schematically in **Figure 1c**. In the first, referred to as the "direct" dissociation of water, two water molecules react directly to form a hydroxide and hydronium ion.

$$2H_2O \underset{k_{-1}}{\overset{k_1}{\rightleftharpoons}} H_3O^+ + OH^- \quad (1)$$

In the above equation, k_1 and k_{-1} are the kinetic rate constants for water dissociation and recombination, respectively. All rate constants, diffusion coefficients, and model parameters are given **Table 2**. For consistency with kinetic rate parameters taken from Craig,[21] this bimolecular water dissociation mechanism is implemented as opposed to a pseudo-unimolecular mechanism that involves a single water molecule splitting into a proton and a hydroxide ion. The equilibrium constants are also reported assuming a molar ratio reference state as opposed to a standard reference state for further consistency with Craig's work (in which species activities are defined

using their molar ratio with respect to the solvent (water) as opposed to their molar concentrations).[21] The thermodynamic consistency of the molar ratio reference state and the bimolecular mechanism are discussed extensively in prior work.[23] The equilibrium constant for the direct pathway is defined as

$$K_1^0 = \frac{k_1}{k_{-1}} = \frac{c_{\mathrm{OH^-}} c_{\mathrm{H_3O^+}}}{c_{\mathrm{H_2O}}^2}, \tag{2}$$

where $c_{\mathrm{OH^-}}$ is the concentration of hydroxide ions, $c_{\mathrm{H_3O^+}}$ is the concentration of hydronium ions, and $c_{\mathrm{H_2O}}$ is the concentration of water.

In the second pathway, referred to as the "acidic" pathway, because it occurs more preferentially in acidic environments. The WD catalyst (*s*–OH) (where *s* represents a catalyst site) is protonated by a water molecule, generating a hydroxide ion; the protonated WD catalyst ($s-\mathrm{OH_2^+}$) is then deprotonated by another water molecule, generating a hydronium ion,

$$\mathrm{H_2O} + s - \mathrm{OH} \underset{k_{-2}}{\overset{k_2}{\rightleftharpoons}} s - \mathrm{OH_2^+} + \mathrm{OH^-} \tag{3}$$

$$\mathrm{H_2O} + s - \mathrm{OH_2^+} \underset{k_{-3}}{\overset{k_3}{\rightleftharpoons}} s - \mathrm{OH} + \mathrm{H_3O^+} \tag{4}$$

The equilibrium constants and rates are taken from directly from Craig *et al.*,[21] and are defined as

$$K_2^0 = \frac{k_2}{k_{-2}} = \frac{c_{s-\mathrm{OH_2^+}} c_{\mathrm{OH^-}}}{c_{\mathrm{H_2O}} c_{s-\mathrm{OH}}}, \tag{5}$$

$$K_3^0 = \frac{k_3}{k_{-3}} = \frac{c_{s-\mathrm{OH}} c_{\mathrm{H_3O^+}}}{c_{\mathrm{H_2O}} c_{s-\mathrm{OH_2^+}}}, \tag{6}$$

where $c_{s-\mathrm{OH}}$ is the concentration of WD catalyst sites, and $c_{s-\mathrm{OH_2^+}}$ is the concentration of protonated WD catalyst sites.

The third pathway considered is referred to as the "alkaline" pathway, because it occurs more preferentially in alkaline environments. The WD catalyst is deprotonated by a water molecule, generating a hydronium ion; the deprotonated WD catalyst (s–O^-) is then protonated by another water molecule, generating a hydroxide ion,

$$H_2O + s - OH \underset{k_{-4}}{\overset{k_4}{\rightleftharpoons}} s - O^- + H_3O^+ \tag{7}$$

$$H_2O + s - O^- \underset{k_{-5}}{\overset{k_5}{\rightleftharpoons}} s - OH + OH^- \tag{8}$$

Similar to the acidic mechanism, the equilibrium constants are defined as

$$K_4^0 = \frac{k_4}{k_{-4}} = \frac{c_{s-O^-}c_{H_3O^+}}{c_{H_2O}c_{s-OH}}, \tag{9}$$

$$K_5^0 = \frac{k_5}{k_{-5}} = \frac{c_{s-OH}c_{OH^-}}{c_{H_2O}c_{s-O^-}}, \tag{10}$$

where c_{s-O^-} is the concentration of deprotonated WD catalyst sites.

Prior research by Onsager[27,28] demonstrated that the equilibrium for reactions that lead to the net generation and consumption of charge are strongly impacted by the local electric field. To incorporate this effect into the simulated WD kinetics, the forward and reverse rates of equations (1), (3), and (7) are modeled as functions of the local electric field. The dependence of the forward rate constant on the electric field is taken directly from work by Lin *et al.* and is given by[11]

$$\frac{k_{i=1,3,7}(E)}{k_{i=1,3,7}^0} = \left(\sum_{m=0}^{\infty} \frac{1}{m!(m+1)!}(2\beta E)^m\right)\cosh(\tau\beta E)\cosh(\tau)^{\,\beta E}. \tag{11}$$

In the above equation, $k_{i=1,3,7}^0$ is the forward rate constant under zero electric field, E is the local electric field, and τ is a lumped parameter:

$$\tau = -0.128\ln(\cosh(0.235\sigma)) + 5.72\sigma^2, \tag{12}$$

where σ is dimensionless bond length defined as the bond length divided by the Bjerrum length.[21]

$$\sigma = \frac{0.58\text{ nm}}{2l_b}, l_b = \frac{\mathrm{e}F}{8\pi\varepsilon_{H_2O}RT} \tag{13}$$

In the above definition, e is the elementary charge, F is Faraday's constant, R is the ideal-gas constant, and T is the absolute temperature. The value of 0.58 nm was derived by Craig[21] and represents the length at which the hydroxide and hydronium ions separate in water. The dependence of the reverse rate constant on the electric field can be determined using the methodology of Onsager,[21]

$$\frac{k_{-1}(E)}{k_{-1}^0} = 1 + \frac{1-\exp\left(-\frac{1}{\sigma}\right)}{2}\left(\sigma^2\beta E + (4.97\sigma)\frac{\sinh(0.0835\sigma\beta E)}{\cosh^2(0.0835\sigma\beta E)}\right) \tag{14}$$

where βE is a dimensionless electric field strength given as

$$\beta E = \frac{l_b F}{2.9RT}E. \tag{15}$$

The value of 2.9 in the dimensionless electric field is used as a dimensionless fitting parameter and dictates the sensitivity of the WD kinetics to the field.[11] As shown in **Figure S2**, the dependence of the forward rate on the electric field is much stronger than that of the reverse rate for high applied electric fields ($\beta E > 1$). Therefore, for the strong electric fields present at the CEL/AEL interface, the forward (dissociation) is accelerated far beyond that of the reverse (recombination) rate.

To characterize various catalysts for WD, the pK_as of the surface reactions on the WD catalyst are typically employed. For the biomolecular surface reactions simulated, these must be scaled by a factor of $\frac{c_{H_2O}^0}{c_{ref}=1\ M}$ = 55 to account for a shift due to treating the concentration of water explicitly (as opposed to just considering water as unit activity)[9] and can be written as

$$\mathrm{pK_2} = -\log_{10}(K_2 \times \frac{c^0_{\mathrm{H_2O}}}{c_{ref}}) \tag{16}$$

$$\mathrm{pK_4} = -\log_{10}(K_4 \times \frac{c^0_{\mathrm{H_2O}}}{c_{ref}}) \tag{17}$$

Oener *et al.* propose the use of the pH at the PZC ($\mathrm{pH_{PZC}}$), defined as the pH where there is a net zero charge on an ionogenic surface.[19] This metric is more useful than the $\mathrm{pK_a}$ because it can be determined experimentally for a transition-metal oxide through the use of zeta-potential measurements.[19,36,37] A more acidic $\mathrm{pH_{PZC}}$ corresponds to an ionogenic surface more likely to be in its deprotonated state (s–$\mathrm{O^-}$). A more alkaline $\mathrm{pH_{PZC}}$ corresponds to an ionogenic surface more likely to be in a protonated state (s–$\mathrm{OH_2^+}$). The $\mathrm{pH_{PZC}}$ can be related to the $\mathrm{pK_a}$s of the surface reactions through the following relationship (see **Section S3** in the Supporting Information for a complete derivation).

$$\mathrm{pH_{PZC}} = 7 + \frac{\mathrm{pK_4} - \mathrm{pK_2}}{2} \tag{18}$$

The homogeneous buffer reactions of phosphate are likely also impacted by the electric field due to the Second Wien Effect. However, because the phosphate titration currents do not constitute a substantially high portion of the current carried beyond the salt-ion plateau region (< 5% for i > 10 mA $\mathrm{cm^{-2}}$)[9], the buffer reactions are neglected from this study. Additionally, the rate enhancements for the Second Wien Effect are determined using atomistic calculations for the dissociation of water, and these parameters are dependent on the choice of dissociating molecule (*e.g.,* the dissociating bond length).[21] These parameters will vary for different dissociating molecules, and the rate enhancement has not yet been quantified for phosphates. The aim of the present study is to understand how the adsorptions of $\mathrm{H^+}$ and $\mathrm{OH^-}$ on the catalyst impact WD, and

while other ions can likely adsorb to the catalyst surface and dissociate in a similar fashion, fully understanding these effects would require further atomistic calculations beyond the scope of the present study. Nevertheless, future work should aim to better understand the interactions between the salt species and the catalyst/electric field.

Fixed charge, catalyst, and water concentration distributions

Consistent with prior studies, the fixed-charge density, catalyst, and water concentration throughout the domain are modeled using hyperbolic tangents,[11,21,23] and are represented below in **Table 1** and discussed in more detail in **Section S4** of the Supporting Information:

Table 1: Concentration distributions employed in the continuum model. See **Section S4** for a detailed discussion of these expressions.

Property	Distribution	Unit	
Membrane Charge	$c_M(x) = \frac{\rho_{M,wet} \times \mathrm{IEC}}{2}\left(\tanh\left(\frac{x-x_3}{L_{char}}\right) - \tanh\left(\frac{x-x_4}{L_{char}}\right) + \tanh\left(\frac{x-x_2}{L_{char}}\right) - \tanh\left(\frac{x-x_1}{L_{char}}\right)\right)$	mol m^{-3}	(19)
Catalyst Concentration	$c^0_{s-\mathrm{OH}}(x) = \frac{\rho_{M,wet} \times \mathrm{IEC}}{2}\left(\tanh\left(\frac{x-x_3}{L_{char}}\right) - \tanh\left(\frac{x-x_4}{L_{char}}\right) + \tanh\left(\frac{x-x_2}{L_{char}}\right) - \tanh\left(\frac{x-x_1}{L_{char}}\right)\right)$	mol m^{-3}	(20)
Water Concentration	$c_{\mathrm{H_2O}}(x) = \frac{c^0_{\mathrm{H_2O}}}{2}\left(2 - \tanh\left(\frac{x-x_1}{L_{char}}\right) + \tanh\left(\frac{x-x_4}{L_{char}}\right)\right) + \frac{c^M_{\mathrm{H_2O}}}{2}\left(\tanh\left(\frac{x-x_1}{L_{char}}\right) - \tanh\left(\frac{x-x_4}{L_{char}}\right)\right)$	mol m^{-3}	(21)

To solve for the distribution of charged sites (*e.g.*, *s*–OH, *s*–O^-, *s*–OH_2^+) within the catalyst layer, the ionogenic surface species are assumed to be immobile, and the mass conservation of these species are solved in conjunction with the site balance to develop analytical expressions for the concentration of each surface species (see **Section S4** for details).

Transport equations

To determine the concentration of all species and electrostatic potential, the following conservation equations were solved. First, the conservation of species (mass),

$$\frac{dN_i}{dx} = R_i. \tag{22}$$

where R_i is the volumetric generation of species i from homogeneous chemical reactions,

$$R_i = \sum_n s_{i,n}\left(k_n \prod_{s_{i,n}<0} c_i^{-s_{i,n}} - k_{-n} \prod_{s_{i,n}>0} c_i^{s_{i,n}}\right), \tag{23}$$

where $s_{i,n}$ is the stoichiometric coefficient of species i in reaction n. N_i is the molar flux of species i defined as

$$N_i = -D_i \frac{dc_i}{dx} + D_i c_i \frac{d\left(\ln\left(c_{\mathrm{H_2O}}\right)\right)}{dx} + z_i D_i c_i \frac{FE}{RT} - D_i c_i \frac{d\left(ln\left(\gamma_{\pm}^{E}\right)\right)}{dx}, \tag{24}$$

where D_i, and z_i are the diffusion coefficient and ionic charge, respectively, of species i. The Nernst-Einstein relation is used to relate mobilities and diffusivities. The diffusion coefficients for a given ionic species are defined to be their binary diffusion coefficients in water for the catholyte and anolyte phases, and the framework developed by Grew *et al.*[38–40] is used to determine the diffusion coefficients in the ionomer phase (see **Section S5**). $\gamma_{\pm}^{E}$ is an electric-field-dependent activity-coefficient term resulting from the Second Wien Effect and only applies to hydronium and hydroxide fluxes, because WD is the only homogeneous reaction affected by the Second Wien Effect in the present study,

$$\gamma_{\pm}^{E} = \sqrt{\frac{k_1^0 k_{-1}(E)}{k_{-1}^0 k_1(E)}} \tag{25}$$

Poisson's equation is solved for the conservation of charge,

$$-\frac{d^2\Phi}{dx^2} = \frac{F}{\varepsilon}\left(c_M(x) + \sum_i z_i c_i\right), \tag{26}$$

where Φ is the electrostatic potential, and ε is the dielectric permittivity of the medium (**Section S6**).

Boundary conditions

As mentioned previously, the nature of the 4-electrode cell enables the use of simplified Dirichlet boundary conditions at each reference electrode. The potential of the Cathode Ref. is set to 0.0 V, and the potential of the Anode Ref. is set to the experimentally applied potential. The concentrations of the ionic species at both references are that of a mixture of 0.45 M K_2HPO_4 and 0.55 M KH_2PO_4 (this will be referred to as 1 M $K_iH_jPO_4$ where i + j = 3 or simply KP_i). In other words, the BPM, as simulated, is immersed in a symmetric, pH-neutral environment based on the bulk pH of the buffer electrolytes used experimentally. This choice of neutral pH is for consistency with prior studies,[11,12,21] which modeled extensively the impact of the pH gradient on the ionic transport.[12,23] Since the purpose of this study is to examine the relative performance of various simulated catalysts to understand property-performance relationships, comparing the applied potentials to achieve WD in a neutral pH electrolyte is sufficient for this goal.

Numerical methods

All equations (species conservation and charge conservation) were modeled in the General Form PDE Module and solved with the PARDISO solver in COMSOL Multiphysics 5.6 with a relative tolerance of 0.001. The modeling domain was discretized with a nonuniform mesh comprised of 1084 elements (see **Figure S7** in the Supporting Information for mesh-independence study), employing exponential refinement near internal phase boundaries to enable convergence and capture sharp concentration gradients. MATLAB Simulink was used with COMSOL 5.6 to

automate data collection, facilitating simulation of WD overpotentials for a wide array of pH_{PZC} WD catalysts.

Table 2: List of model parameters and their source.

Parameter	Value	Unit	Ref.
Membrane			
L_{AEL}	80	μm	35
L_{CEL}	80	μm	35
IEC	1.81	mmol g^{-1}	[41] (Fumatech)
	1.01		[42] (Nafion)
$\rho_{M.wet}$	1.0	g mL^{-1}	35 (Fumatech)
	1.65		[43] (Nafion)
L_{char}	0.58	nm	21
$\lambda_{f_{H_3O^+}=1}$ and $\lambda_{f_{OH^-}=1}$	12		[41] (Fumatech)
	22		[44] (Nafion)
L_{CL}	10	nm	11
	200		19
Electrolytes			
L_{aBL}	20	μm	Assumed
L_{cBL}	20	μm	Assumed
$c^0_{H_2O}$	55.56	mol L^{-1}	21
Aqueous Transport Properties			
$D_{K^+,w}$	1.96×10^{-9}	m^2 s^{-1}	[45]

$D_{HPO_4^{2-},w}$	6.9×10^{-10}	$m^2\ s^{-1}$	[45]
$D_{H_2PO_4^-,w}$	8.46×10^{-10}	$m^2\ s^{-1}$	[45]
$D_{H_3O^+,w}$	6.96×10^{-9}	$m^2\ s^{-1}$	21
$D_{OH^-,w}$	4.96×10^{-9}	$m^2\ s^{-1}$	21
ε_{H_2O}	6.934×10^{-10}	$F\ m^{-1}$	21
ε_M	1.96×10^{-11}	$F\ m^{-1}$	21
Homogeneous Reactions			
K_1^0	3.26×10^{-18}		21
k_1^0	2.96×10^{-10}	$m^3\ (s\ mol)^{-1}$	21
k_{-1}^0	9.08×10^{7}	$m^3\ (s\ mol)^{-1}$	21
K_2^0	3.9×10^{-6}		11
k_2^0	83.959	$m^3\ (s\ mol)^{-1}$	11
k_{-2}^0	2.13×10^{7}	$m^3\ (s\ mol)^{-1}$	11
K_3^0	8.36×10^{-13}		11
k_3^0	1.8×10^{-5}	$m^3\ (s\ mol)^{-1}$	11
k_{-3}^0	2.15×10^{7}	$m^3\ (s\ mol)^{-1}$	11
K_4^0	3.9×10^{-6}		11
k_4^0	83.959	$m^3\ (s\ mol)^{-1}$	11
k_{-4}^0	2.13×10^{7}	$m^3\ (s\ mol)^{-1}$	11
K_5^0	8.36×10^{-13}		11
k_5^0	1.8×10^{-5}	$m^3\ (s\ mol)^{-1}$	11

k^0_{-5}	2.15×10^7	m^3 $(s\ mol)^{-1}$	11
K_6	1.116×10^{-9}		46
k_{-6}	10×10^{11}	M^{-1} s^{-1}	47

Results and discussion

Model validation

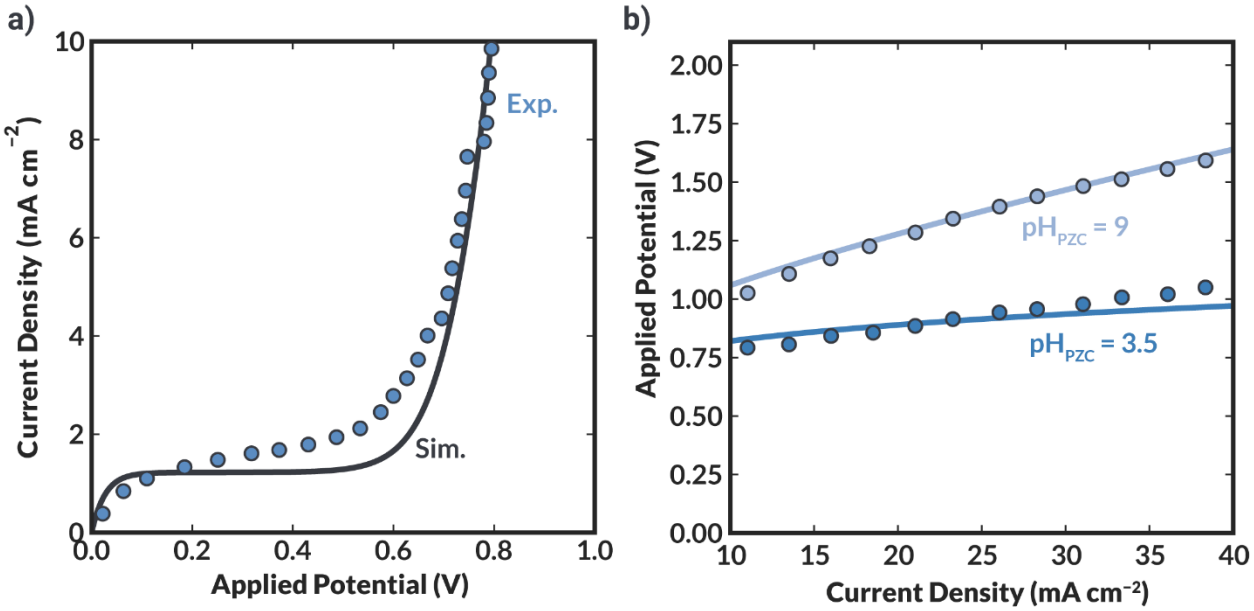

Figure 2: Model validation: **(a)** Fit of experimental polarization data from Vermaas *et al.*[12] for a 4-probe experiment performed with 1 M potassium phosphate electrolyte. **(b)** Fit of experimental data from Oener *et al.*[19] in a membrane-electrode assembly with pure water feeds at both electrodes; the experimental data are shifted by a constant fit value of 0.82 V to account for ohmic and kinetic overpotentials not modeled in the 4-probe simulation.

Table 3: Fitted parameters for Vermaas *et al.*[12] and Oener *et al.*[19] data.

Dataset	Parameter	Value	Units
Vermaas *et al.*[12]	$\lambda_{f_{H_3O^+}=0}$ and $\lambda_{f_{OH^-}=0}$	6	
Vermaas *et al.*[12]	pK_2	4	
Vermaas *et al.*[12]	pK_4	10	

Oener *et al.* [19]	$\lambda_{f_{H_3O^+=0}}$ and $\lambda_{f_{OH^-=0}}$	14.5	
Oener *et al.* [19]	$V_{faradaic}$	0.82	V
Oener *et al.* [19]	m_i	$\frac{4D_{i,w}z_iF}{RT}$	$m^2\ V^{-1}\ s^{-1}$

First, the model was validated for an experimental dataset of Fumatech BPM performance reported by Vermaas *et al.*,[12] in which the salt-exchanged water uptake, and catalyst pK_a values constituted the three fitted parameters (**Figure 2a** and **Table 3**). The catalyst pK_a values were used to fit the exponential onset potential for WD, and the salt-exchanged water uptake was used to fit the salt-ion crossover plateau current. The salt-exchanged water uptake value of 6 is also consistent with prior study by Bui *et al.*,[9] and the catalyst pK_as are consistent with those fit by Craig.[21] Sensitivity to the salt-exchanged water uptake is shown in **Figure S8**, and the sensitivity to the pK_as are discussed later**.** There exists slight disagreement in the salt-ion crossover plateau regime that is likely due to the neglecting of the buffer reactions in the study. As shown in **Figure S9**, when source terms associated with the buffer reactions are considered, the fit improves within the salt-ion plateau. However, as expected, beyond the salt-ion plateau, the simulation can adequately predict experimental behavior because the titration currents are minor in the WD regime. This result further demonstrates that, within the WD regime of interest,

Next, experimental polarization curves of BPMs with two different 200 nm thick CLs developed by Oener *et al.*[19] were simulated. Contrary to the Vermaas *et al.* data, the pH_{PZC} of each CL was known, so pK_as were chosen to match the desired pH_{PZC} and were not considered fitting parameters because at a given pH_{PZC}, the model was found to be relatively insensitive values of the individual pK_as (**Figure S10**). Therefore, the fitting parameters for this set of BPMs were the salt-ion exchanged water content, a voltage shift to account for Faradaic reactions in the two-

electrode experiment, and the mobility of ions within the WD CL (**Table *3***). The choice of salt-exchanged water uptake is consistent with that measured experimentally.[48] Sensitivity to the salt-exchanged water uptake and ionic mobility are shown in **Figures S11-12.** The experimentally measured potentials were shifted to fit the model because the simulation is modeling a 4-probe cell, whereas the experimental study utilized a zero-gap MEA with pure water fed on both sides and no reference electrodes. Therefore, there are additional overpotentials (*i.e.*, the kinetic overpotentials at the anode and cathode, ohmic losses, *etc.*) in the experiment that are not captured in the simulation. Moreover, the streaming potentials resulting from co- and counter- ion crossover in the simulation are subtracted from the simulated polarization curve, because these ions are not present in a water-fed MEA. Additionally, to fit the curves, the ion mobilities had to be increased 4× with the same diffusivities. This implies that the Nernst-Einstein relationship is not valid within the junction, which is reasonable due to the concentrated nature of ionic interactions there.[49,50] Strong agreement can be achieved for both polarization curves for the Oener CLs of distinct pH_{PZC} fit with a single set of fit parameters (**Table *3*** and **Figure 2b**). As simulated, moving from a pH_{PZC} of 3.5 to a pH_{PZC} of 9 results in an approximately 300 mV shift in the required overpotential for WD at 10 mA cm^{-2}, consistent with the experimental data.[19] The fitting parameters employed to fit the Oener set of BPMs differed from those used to fit the data from Vermaas *et al.*[12] However, this difference is to be expected because the BPMs in each study are comprised of completely different polymer chemistries. The Vermaas study employed a commercial Fumatech FBM[12], whereas the Oener study employed a custom-fabricated BPM made from Nafion and Sustainion[19].

The impact of pH_{PZC} on WD performance

The model was exercised to help elucidate the mechanism of WD in BPM junctions and understand better the factors dictating WD catalyst performance in BPMs. Systematic simulations

were conducted by varying the value of the k_2 and k_4 (and thus pK_2 and pK_4), for 400 unique combinations of pK_2 and pK_4, and the applied membrane potential required to achieve a current density of 15 mA cm^{-2} was calculated starting from the base fits of the Vermaas *et al*. data. The applied membrane potential required to achieve the target current density of 15 mA cm^{-2} in these simulations serves as a useful metric to evaluate various WD catalysts. The results of the simulation are shown in **Figure 3**.

Figure 3a depicts the membrane potential required to achieve 15 mA cm^{-2} plotted against the pK_2 and pK_4 in a 3D-contour plot. The color shading of the contour plot describes the acidity or alkalinity of the pH_{PZC}. As depicted, it becomes clear that WD kinetics improve as the pH_{PZC} of the catalyst becomes more acidic or alkaline; catalysts with neutral pH_{PZC} perform the poorest. Additionally, when polarization curves are plotted for catalysts of varying pH_{PZC} (**Figure 3b**), it is further demonstrated that the performance improves substantially with increasing acidity or alkalinity. The improvement in performance with increasing acidity or alkalinity is relatively symmetric about a neutral pH_{PZC} catalyst, which is likely a result of the symmetric choice of background charge in the modeled BPM. The findings of the simulation are consistent with prior experiments performed by Oener *et al.*, who demonstrated a similar correlation between the acidity or alkalinity of a catalyst's pH_{PZC} and its WD performance.[19]

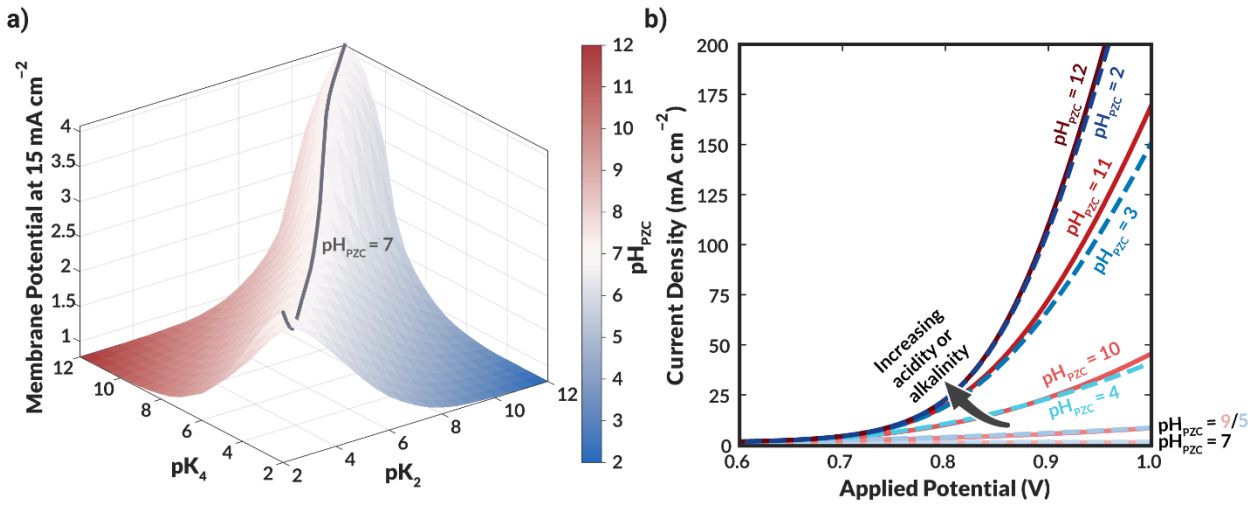

Figure 3: (a) Contour plot depicting the correlation between the pH_{PZC} and the applied membrane potential required to achieve a current density of 15 mA cm^{-2}. The x-axis is pK_2, the y-axis is pK_4, the z-axis is the applied membrane potential, and the color of the contour corresponds to the pH_{PZC} of the WD catalyst calculated using eqn (18). **(b)** Polarization curves of WD catalysts for varying pH_{PZC}. For red (alkaline) curves, pK_2 was held at a value of 2, and pK_4 was varied from 2 to 12. For blue (acidic) curves, pK_2 was held at a value of 12, and pK_4 was varied from 12 to 2.

Interfacial concentration and electric-field profiles at the CEL/AEL junction

To understand better the mechanism of catalytically enhanced WD performance, it is illustrative to consider interfacial concentration profiles of the protonated and deprotonated sites, as well as the concentrations of hydronium and hydroxide ions. These profiles are shown in **Figure 4a-f** for an applied membrane potential of 1 V (see **Figures S13-14** for these profiles at applied voltages of 0.0 V and 0.5 V of applied membrane potential). As expected, the distribution of charged sites in the CL differ substantially as the pH_{PZC} of the CL is made more alkaline or acidic (**Figure 4a-c**).

For a neutral pH_{PZC}, the distribution of sites is symmetric, with a buildup of charged catalyst species at each side of the CL. $s{-}OH_2^+$ species build up at the interface of the CEL and CL, and $s{-}O^-$ species build up at the interface of the CL and AEL. Within the interior of the CL, the concentration of $s{-}OH_2^+$ and $s{-}O^-$ are approximately equivalent (**Figure 4a**). The existence

of this catalyst site distribution can be rationalized when considering the concentration profiles of hydronium and hydroxide within the junction region (**Figure 4d**). At the high applied membrane potentials where WD takes place, hydronium ions form in the CL and exit out the CEL. Similarly, hydroxide ions form in the CEL and exit out the AEL. This phenomenon leads to a high concentration of hydronium at the CEL/CL interface, and a high concentration of hydroxide at the CL/AEL interface. Thus, following the equilibrium of the ionogenic surface reactions, the high concentration of hydronium ions at the CEL/CL interface leads to a buildup of positively charged $s{-}OH_2^+$ sites at that interface. At the CL/AEL interface, the concentration of hydroxides drives the alkaline pathway and thus enables an equivalent buildup of $s{-}O^-$ sites.

Conversely, for an acidic or alkaline pH_{PZC}, the distribution of sites is skewed. For the acidic pH_{PZC}, there is a significantly larger buildup of $s{-}O^-$ sites at the CL/AEL interface than of $s{-}OH_2^+$ sites at the CEL/CL interface (**Figure 4e**). For the alkaline pH_{PZC}, there is a larger buildup of $s{-}OH_2^+$ sites at the CEL/CL interface than of $s{-}O^-$ sites at the AEL/CL interface (**Figure 4f**). These skewed site distributions are a result of the asymmetric equilibria of the ionogenic surface reactions. Because an alkaline pH_{PZC} catalyst is more likely to hold a positive charge, it more preferentially forms $s{-}OH_2^+$ sites. Similarly, an acidic pH_{PZC} catalyst is more likely to hold a negative charge, and thus more preferentially forms $s{-}O^-$ sites.

The skewed site distributions simulated in acidic or alkaline pH_{PZC} WD catalysts can be used to understand their improved performance. For an acidic or alkaline pH_{PZC} catalyst, the maximum density of fixed charges at the interface between the ion-exchange layers and the CLs is increased when compared against the neutral pH_{PZC} case. Because the electric field is dependent on the gradient in fixed charge, the increase in the interfacial fixed charge density also corresponds to an increase in the maximum achieved electric field. At the CEL-CL interface, there is a large

gradient in fixed charge going from the negative fixed charge groups in the CEL to the positive $s-OH_2^+$ group in the CL. At the CL-/AEL interface, the gradient goes from the negative $s-O^-$ groups in the CEL to the positive fixed charge groups in the AEL. The skewed site distribution maximizes this gradient, and thus the electric field. The electric field strength in the acidic or alkaline case achieves a maximum value of 3 compared to the value of 2 in the neutral case. Although the neutral pH_{PZC} case enables a field strength of 2 on both side of the CL, whereas the acidic and alkaline achieve values of 1 and 3; because the Second Wien Effect operates on an approximately exponential dependence, the difference in the WD rate going from a field strength of 2 to 3 is an enhancement of 10^4 (**Figure S2**). This hypothesis is corroborated by examining the interfacial electric field profiles at a galvanostatic applied current density of 100 mA cm^{-2}. As shown in **Figure S15**, at a constant current density across the neutral, acidic, and alkaline catalysts, a nearly identical maximum electric field strength of ~3 is achieved for all catalysts. This finding demonstrates that the attainment of high electric field in the catalyst layer dictates the achievable WD current density. This substantial enhancement in the WD rate for the skewed electric-field distribution explains the improved performance for acidic and alkaline pH_{PZC} WD catalysts.

This finding ultimately leads to a mechanistic understanding of the enhanced performance for WD witnessed with transition-metal-oxide catalysts, as they screen the electric field through the generation of fixed charged species within the CL. This results also demonstrates that WD occurs primarily at the interface of the ionomer and the CL, not necessarily within the bulk of the CL, consistent with prior simulation studies.[11,21] However, in the prior work investigating the formation of charged species in the BPM junction, only the acidic pathway was considered.[11,21] Because of the omission of the alkaline pathway, it was suggested that all WD occurred at the interface of the CEL and CL, and that WD performance could be enhanced simply by reducing the

pK_2 of the WD catalyst to facilitate the formation of more $s{-}OH_2^+$, enhancing the fixed charge gradient and thus the field enhancement of the WD.[11] The present study demonstrates that the pH_{PZC}, not the pK_a, is a reliable metric to characterize the activity of WD catalysts, and that the location of the WD reaction depends on the pH_{PZC}. Additionally, the work demonstrates that the field-enhanced WD occurs only at the ion-exchange layer/CL interface, not throughout the CL as a whole, as has been suggested in prior work.[9,19]

Interestingly, when breaking down the contributions of the polarization curve due to the acidic, alkaline, and direct WD pathways, the polarization behavior is primarily controlled by the direct WD pathway (see **Figure S16**). This result is also consistent with prior studies.[11,21] However, in the work by Craig *et al.*, it was posited, that because the WD was dominated by the direct pathway, the WD catalyst was not active or necessary for enhanced WD performance.[21] Lin *et al.* refuted this claim, claiming that even though the direct pathway is preferred, the WD catalyst is necessary to develop the electric fields that accelerate WD in BPMs.[11] This latter theory is consistent with our findings. Nevertheless, these results imply that a BPM without a catalyst and simply a zero gap would exhibit the greatest WD performance; however, many prior studies have demonstrated that BPMs in this zero-gap configuration without a WD catalyst perform quite poorly.[16,19] This discrepancy in performance between theory and experiment is likely due to the mobility and condensation of charges present in the ion-exchange layers. As simulated, the charged side groups in the ion-exchange layer are simulated as immobile. In practical application, the charges on the oppositely charged ionomers are slightly mobile and can condense, limiting the fixed charge gradient and electric field achievable in a BPM without a CL that provides more inherent charge separation.[44,49,51,52] Conversely, surface charges on a metal oxide are likely less mobile and enable the buildup of a larger field for WD.

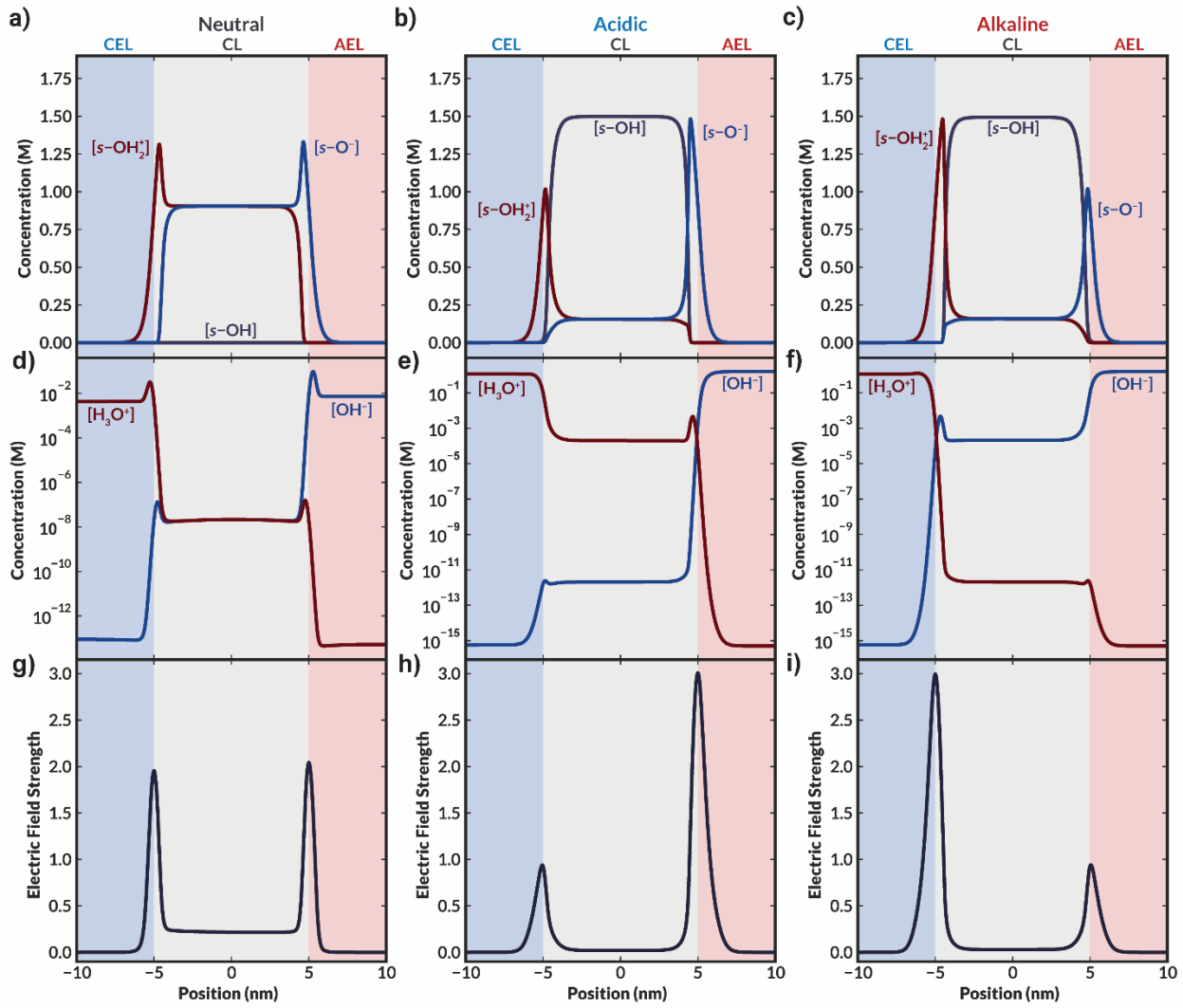

Figure 4: Interfacial profiles for CLs of varying pH_{PZC}. **(a-c)** Distribution of charged catalyst surface sites. **(d-f)** Hydronium and hydroxide concentration. **(g-i)** Dimensionless electric-field strength as defined in Eq (15). The WD catalyst in **(a, d, g)** has a $pH_{PZC} = 7$ ($pK_2 = pK_4 = 2$), the WD catalyst in **(b, e, h)** has $pH_{PZC} = 3$ ($pK_2 = 10$, $pK_4 = 2$), and the WD catalyst in **(c, f, i)** has $pH_{PZC} = 11$ ($pK_2 = 2$, $pK_4 = 10$). All profiles shown are simulated at an applied membrane potential of 1.0 V. See **Figures S11-12** in the Supporting Information for profiles at lower applied potentials.

Sensitivity analysis of WD performance

Now that the mechanism of field-enhanced WD in the BPM junction is understood better, a sensitivity analysis of WD can be performed to optimize performance of the WD CL. For these sensitivity analyses, the fit membrane properties from the Vermaas *et al.* dataset were employed

(**Table 3**). However, the pH_{PZC} was shifted to 11 (pK_2 = 2, pK_4 = 10), which represents a more optimal catalyst material, to demonstrate how properties of the BPM beyond the choice of WD catalyst can impact the WD current density observed. First, the ion-exchange capacity (IEC) (defined as the molar equivalents of fixed-charge groups per gram of membrane) was varied while holding all other properties constant. As depicted in **Figure 5a**, increasing the IEC can enhance WD performance, as has been reported in prior studies.[11,23] This increase results from the increase in fixed-charged groups enhancing the local field at the CEL/CL interface. However, unlike what has been shown in prior studies, at higher values of the IEC, the WD current density achieved by the BPM decreases (IEC > 2.5 meq g^{-1} see **Figure S17**). This behavior arises because of the dependence of the water content on the IEC, which prior studies that have modeled interfacial behavior have neglected.[11,21] As the water content increases, the dielectric permittivity of the junction increases (see **Figure S18**).[53,54] The WD performance is highly sensitive to the dielectric permittivity in the junction region (see **Figure S19**). As the permittivity in the junction decreases, the gradients in electric field as determined by Poisson's equation decrease (eq (26)). This analysis presents an interesting performance trade-off regarding the design of BPMs: an optimal BPM should possess a high IEC to enhance the field, but not so high that the subsequent increases in the dielectric permittivity prevent the proper screening of that field.

Next, the concentration of catalyst sites was varied holding all other parameters constant. As demonstrated in **Figure 5b**, the performance of the BPM improves when the concentration of sites in the CL is increased. However, there is a point beyond which further increases in the site concentration do not result in increases in current density at the applied potential (**Figure S21**). The model suggests that this behavior results from competing phenomena that occur when the total site concentration is increased. When the number of available catalyst sites increases, the ability

for the catalyst to form charged $s{-}OH_2^+$ species increases. This increase in charged $s{-}OH_2^+$ species increases the local field at the CEL/CL interface and enhances WD. However, the increase in $s{-}OH_2^+$ species also traps more generated OH^- species at the CEL/CL junction through electrostatic interactions (see **Supporting Figure S22**). These trapped OH^- species can recombine with the H_3O^+ species in the CEL, increasing the rate of recombination by mass action (see **Supporting Figure S23**). Therefore, there reaches a point where the increases in dissociation due to the enhanced field from the greater number of charged groups are offset by increases in parasitic recombination due to the greater capacity of the CL to hold OH^- ions.

Interestingly, the greatest enhancements in performance can be seen when the IEC and catalyst site concentration are both increased by a commensurate amount, due to the increase in the interfacial field resulting from the increased amount of fixed charge on both sides of the CEL/CL interface (see **Supporting Figure S24**). However, these enhancements will also eventually be limited. If the IEC is enhanced too far, the mechanical integrity of the ion-exchange layer will be compromised.[42] Furthermore, while the porosity (the void volume for which electrolyte can transport) of the CL is kept constant in this study, if the concentration of catalyst sites becomes too large, the porosity of the CL will eventually become too small to support ionic transport. Therefore, there is an intrinsic limit to how much the WD performance can be enhanced by increasing the fixed-charge concentrations.

Lastly, the CL thickness was varied holding all other parameters constant. As demonstrated in **Figure 5c**, increasing the CL thickness decreases its performance. This decrease in performance with increasing thickness has been reported previously.[9,11,22] However, unlike prior studies that demonstrate extreme sensitivity to thickness with CLs having to be less than 10 nm in thickness to achieve modest current densities,[22,23] the model presented herein achieves substantial WD

current density even at a thickness of 100 nm. The reduced sensitivity of this model to CL thickness results from the fact that WD is localized to the CEL/CL interface; therefore, the thickness of the CL has relatively minimal impact on the catalyst utilization. The present model demonstrates that the observed sensitivity to CL thickness is due to increased ohmic resistance of the CL with increasing thickness—WD-generated hydronium or hydroxide ions that must transport through the junction are transport limited with increasing junction thickness. As shown in **Supporting Figure S25**, as the CL thickness is increased, the potential drop or ohmic loss across the CL also increases, thereby providing less potential to drive WD at the CEL/CL interface.

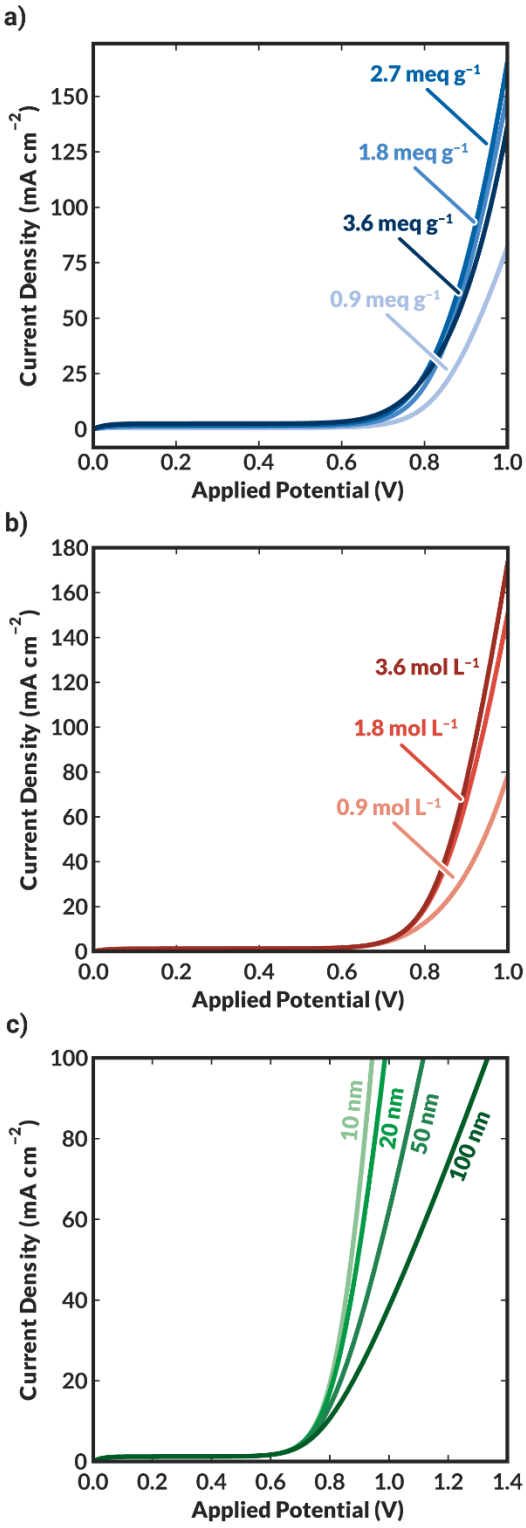

Figure 5: Sensitivity analysis of BPM polarization curves to various catalyst layer and membrane properties: **(a)** Ion-exchange capacity, **(b)** catalyst site ($s-$OH) concentration, and **(c)** CL thickness.

Understanding Performance of Bi-metallic WD Catalysts

Lastly, recent developments in novel bi-metallic catalysts for water splitting,[55,56] CO_2 reduction,[57–59] as well as for interfacial WD in BPMs,[19] have led to intense discussion on the mechanistic properties of these bi-metallic catalysts. The model developed herein can be used to elucidate the electrochemical behavior of the bi-metallic WD catalysts recently employed in BPMs. As demonstrated in prior study,[19] the pairing of a bi-metallic WD catalyst's pH_{PZC} with the adjacent ion-exchange layer can be used to prescribe its electrochemical performance. When a catalyst with an acidic pH_{PZC} is paired with the CEL and a catalyst with an alkaline pH_{PZC} is paired with the AEL, far superior performance can be achieved than for the case with the opposite pairing (**Figure 6a**). Intriguingly, this behavior directly contradicts previous simulations by Wrubel *et al.,* which suggested that an alkaline catalyst should be paired with the CEL, and an acidic catalyst should be paired with the AEL.[34] However, in that work, fixed-charge groups were modeled as dispersed uniformly throughout the CL, and, in this work, the catalyst exists as a distinct layer, potentially explaining the discrepancy. Nonetheless, the improved performance upon pairing the CEL with an acidic pH_{PZC} CL and the AEL with an alkaline pH_{PZC} CL is consistent with recent experimental work by Oener *et al.* that systematically tested various bi-metallic WD catalyst pairings.[19] They proposed that the reason for the improved performance was that for WD catalysts possessing pH_{PZC} matching the pH of the adjacent ion-exchange layer, there would exist a large diversity of surface-protonation sites that would be necessary to drive the reaction steps in the acidic or alkaline WD mechanism at the CEL or AEL, respectively.[19] The simulations herein contradict this explanation, because, as was shown for the monometallic case, WD in the BPM junction occurs primarily through the direct mechanism, not the acidic or alkaline mechanism as previously hypothesized

(**Figure S28**). Therefore, there must exist an alternative explanation for the enhanced performance of bi-metallic catalysts with the demonstrated optimal pH_{PZC} matching.

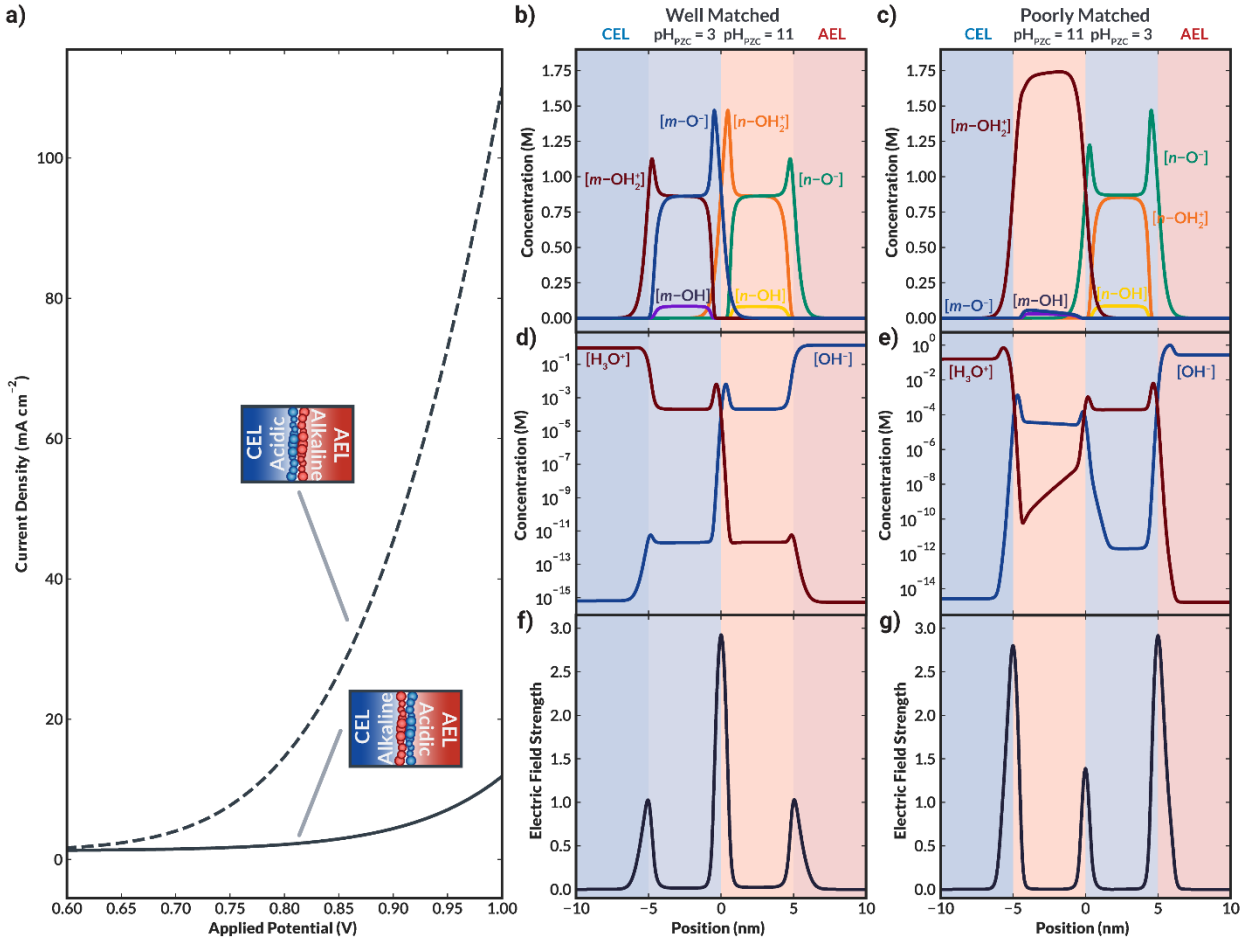

Figure 6: (a) Simulated Electrochemical behavior of BPMs employing bi-metallic WD catalysts. **(b-g)** Interfacial profiles for CLs of varying pH_{PZC}. **(b-c)** Catalyst-site concentration distributions. **(d-e)** Hydronium and hydroxide concentration. **(f-g)** Electric-field strength. The WD catalyst in **(b, d, f)** is well-matched, with the pH_{PZC} matched to the adjacent ion-exchange layer's pH. The WD catalyst in **(c, e, g)** is poorly matched, with the pH_{PZC} opposite of the adjacent catalyst layer's pH. All profiles shown are simulated at an applied membrane potential of 1.0 V. See **Figures S26-27** in the Supporting Information for profiles at lower applied potentials.

Examining the interfacial junction concentration profiles again elucidates the mechanism of enhancement for WD in BPMs employing bi-metallic WD catalysts (**Figure 6b-g**). For the case of the well matched bi-metallic catalyst (CEL-Acidic-Alkaline-AEL), the highly acidic nature of the WD catalyst leads to a buildup of negatively charged, deprotonated surface species at the

interface of the two different metal catalysts (acidic/alkaline). At the CEL/acidic pH_{PZC} catalyst interface, the high concentration of protons leads to a buildup of positively charged, protonated surface species. However, this buildup of positive charges is modest due to the equilibrium of the acidic pH_{PZC} catalyst favoring negatively charged surface species. The reverse occurs at the side with the alkaline pH_{PZC} catalyst, with a large buildup of protonated species at the interface of the two catalysts, and a modest buildup of deprotonated species at the interface of the AEL and the catalyst. Contrary to what was demonstrated for the monometallic catalysts, where WD occurred primarily at the interface of the ion-exchange layers and the catalyst, WD for the bi-metallic occurs primarily at the interface of the two distinct catalyst species (*i.e.*, at the direct center of the CL).

The performance of the poorly matched bi-metallic catalyst is somewhat nonintuitive, especially when considering the results shown for the monometallic catalyst. The buildup of charge matches what would be expected from examination of the monometallic case, positively charged surface species build up at the interface of the CL with the CEL and negatively charged species build up at the interface of the CL with the AEL. This buildup of charges creates large fields at both interfaces, and the presence of two regions of large field of similar magnitude to the well-matched case would imply better performance for the poorly matched case. However, while WD does occur at the interface of the ion-exchange layers and the CL, a significant degree of recombination occurs at the interface of the two catalysts, similar to what is shown above when increasing the concentration of catalyst sites (see **Figure S29**). The recombination observed in the poorly matched case can be rationalized as follows. Hydronium ions generated at the AEL/CL interface must transport through the CL to reach the CEL, and hydroxide generated at the CEL/CL interface must transport through the CL to reach the AEL to transport out of the junction. Because there is WD from both sides, hydroxide and hydronium are both transporting through the CL, and

they recombine at the interface due to mass action. This parasitic recombination reduces the WD current density achievable in the poorly matched case, and is similar to electron/hole recombination observed in semiconductors. Additionally, because hydronium has greater transport properties than hydroxide, the recombination reaction is limited by hydroxide, leading to excess hydronium in the alkaline pH_{PZC} CL, which rapidly protonates the surface oxide. The excess of hydronium explains the asymmetric profiles observed in **Figure 6c** and **e**.

Interestingly, when comparing performance of the well-matched bi-metallic WD catalyst to that of a monometallic catalyst, the monometallic catalyst requires less overpotential to achieve similar current densities (**see Figure S30**). This behavior is not what is observed experimentally[19] but could also be a result of the lack of side-chain mobility within the current model. A key distinction of the well-matched bi-metallic WD catalyst is that it relocates the area of strongest field from the CL/ion-exchange layer interface to the interface between the two oppositely charged catalysts. Therefore, the field in the case of the bi-metallic catalyst would not be neutralized by the mobility of the polymer sidechains, and this could explain the higher current densities observed experimentally. Further model development should seek to confirm this theory by accounting for polymer mobility in the determination of the local electric fields.

Conclusions

Bipolar membranes (BPMs) present immense opportunity to assist in the development of electrochemical devices with optimal pH environments for electrochemical synthesis applications. However, their applicability has long been limited by the substantial applied voltages required for the water-dissociation (WD) catalyst at the interface of the cation- and anion-exchange layers (CEL and AEL). In the present study, a continuum model of the BPM is developed that explicitly models the WD catalyst and exhibited good agreement across multiple experimental datasets. The

model demonstrates that WD catalysts with more highly alkaline or acidic pH_{PZC} exhibit substantially improved WD kinetics, due to their ability to easily hold surface charge and thus screen the electric field. Sensitivity analysis of the model demonstrates that the BPM performance is positively sensitive to the AEL and CEL ion-exchange capacity (IEC) for low values of the IEC, but negatively sensitivity at higher values of the IEC, because the enhanced water content at high values of the IEC increases the dielectric permittivity of the junction region, lowering the electric field. Additionally, the BPM is shown to be highly sensitive to the catalyst site concentration, but only up to a certain point, whereupon enhanced recombination offsets enhancements in the field. Regarding the CL thickness, thinner BPMs are shown to be ideal, because the ohmic losses through thicker CLs inhibit WD. Lastly, the model is employed to study bi-metallic WD catalysts, rationalizing experimental findings that the optimally matched bi-metallic WD catalyst has an acidic pH_{PZC} catalyst adjacent to the CEL and an alkaline pH_{PZC} catalyst adjacent to the AEL.

Future work should aim to implement the developed physics into full-cell MEA-type models that can achieve high current densities (> 1 A cm^{-2}) for which the explicit treatment of membrane-species, and species-species interactions will become more relevant.[18,19,60–62] Additionally, a real catalyst likely has a range or spectrum of surface sites each with distinct pK_as,[63,64] whereas only protonated and deprotonated sites are considered in this model. Co-ion and counter-ion adsorption in the CL were also neglected in this study, owing to the lack of data regarding physical rate constants for these adsorption processes. Detailed quantum chemical calculations or novel experiments will be required to elucidate the impact of these variables. Therefore, future work in modeling BPMs should aim to develop multi-scale models that capture surface adsorption and polymer dynamics on both a continuum and molecular scale. The inclusion of these phenomena may explain key discrepancies between the model and experimental study,

such as the poorer predicted performance of the bi-metallic catalyst than the monometallic catalyst. Nonetheless, the present model describes well the impacts of pH_{PZC} for a theoretical monometallic and bi-metallic WD catalyst and provides substantial insight into the mechanism of field-assisted WD that has been heretofore missing from discussion of BPMs and will be useful for the future design and study of catalysts for BPM WD.

Acknowledgements

We would like to thank Prof. Clay Radke, Prof. Shannon Boettcher, and Prof. Shane Ardo for fruitful discussions in the preparation of this manuscript. This material is based on work performed by the Liquid Sunlight Alliance, which is supported by the U.S. Department of Energy, Office of Science, Office of Basic Energy Sciences, Fuels from Sunlight Hub under Award Number DE-SC0021266. JCB acknowledges funding from the National Science Foundation Graduate Research Fellowship under Grant No. DGE 1752814. JCB acknowledges funding in part by a fellowship award through the National Defense Science and Engineering Graduate (NDSEG) Fellowship Program sponsored by the Army Research Office (ARO).

Associated Content

Supporting Information

The Supporting Information is available free of charge on the ACS Publications website at DOI: XXXX

- Model sensitivity to electrolyte boundary-layer thickness; sensitivity of rate constants to electric field; derivation of pH_{PZC} definition; fixed-charge, catalyst site, and initial water concentration distributions; ionic species diffusion coefficients; permittivity distribution; mesh independence study; sensitivity of Vermaas polarization curves to fit parameters; sensitivity of polarization curves to inclusion of phosphate buffer source terms; sensitivity of Oener polarization curves to fit parameters; sensitivity of polarization curves to individual pK_as at a given pH_{PZC}; junction profiles at different applied voltages for monometallic catalysts; interfacial electric field profiles for various pH_{PZC} catalysts at 100 mA cm^{-2}; breakdown of water dissociation current by contribution by each pathway; ion-exchange capacity sensitivity; catalyst site concentration sensitivity; catalyst-layer thickness sensitivity; junction profiles at different applied voltages for bi-metallic catalysts

Nomenclature

Roman

c_i	Concentration of species i (M)
D_i	Diffusivity of species i ($m^2\ s^{-1}$)
E	Electric field ($V\ m^{-1}$)
e	Elementary charge
F	Faraday constant
G	Gibbs free energy ($J\ mol^{-1}$)
IEC	Ion Exchange capacity ($mmol\ g^{-1}$)
k_B	Boltzmann constant
K_n	Equilibrium constant in reaction n
k_n	Forward rate constant of reaction n
L	Length (m)
l_B	Bjerrum Length (m)
M_i	Molar mass of species i ($g\ mol^{-1}$)
N_i	Molar flux of species i ($mol\ m^{-2}\ s^{-1}$)
R	Ideal gas constant ($J\ mol^{-1}\ K^{-1}$)
R_i	Source term for species i ($mol\ m^{-3}\ s^{-1}$)
$s_{i,n}$	Stoichiometric coefficient of species i in reaction n
T	Temperature (K)
x	1-dimensional position variable (m)
z_i	Charge of ion i

Greek

β	Non-dimensional electric field scaling factor ($m\ V^{-1}$)
ε	Dielectric permittivity ($F\ m^{-1}$)
λ	Water content
μ	Chemical potential of species i ($J\ mol^{-1}$)
ξ	Species-membrane/Species-water diffusivity ratio
ρ	Density ($g\ cm^{-3}$)
σ	Dimensionless dissociation bond length
Φ	Electrostatic potential (V)
ϕ	Ionomer water volume fraction

Subscript

$char$	Characteristic
eff	Effective
i	Ionic species
M	Value in membrane

w	Value in water

Superscript

0	Intrinsic value or standard state
E	Electric field dependence

Acronyms

AEL	Anion exchange layer
BPM	Bipolar membrane
CEL	Cation exchange layer
CL	Catalyst layer
PZC	Point of zero charge
WD	Water dissociation

References

(1) Gabrielsson, E. O.; Tybrandt, K.; Berggren, M. Ion Diode Logics for pH Control. *Lab Chip* **2012**, *12* (14), 2507–2513. https://doi.org/10.1039/c2lc40093f.

(2) Blommaert, M. A.; Aili, D.; Tufa, R. A.; Li, Q.; Smith, W. A.; Vermaas, D. A. Insights and Challenges for Applying Bipolar Membranes in Advanced Electrochemical Energy Systems. *ACS Energy Lett.* **2021**, *6*, 2539–2548. https://doi.org/10.1021/acsenergylett.1c00618.

(3) Vargas-Barbosa, N. M.; Geise, G. M.; Hickner, M. A.; Mallouk, T. E. Assessing the Utility of Bipolar Membranes for Use in Photoelectrochemical Water-Splitting Cells. *ChemSusChem* **2014**, *7* (11), 3017–3020. https://doi.org/10.1002/cssc.201402535.

(4) Luo, J.; Vermaas, D. A.; Bi, D.; Hagfeldt, A.; Smith, W. A.; Grätzel, M. Bipolar Membrane-Assisted Solar Water Splitting in Optimal pH. *Adv. Energy Mater.* **2016**, *6* (13), 1–7. https://doi.org/10.1002/aenm.201600100.

(5) Li, Y. C.; Lee, G.; Yuan, T.; Wang, Y.; Nam, D. H.; Wang, Z.; Garciá De Arquer, F. P.; Lum, Y.; Dinh, C. T.; Voznyy, O.; Sargent, E. H. CO_2 Electroreduction from Carbonate Electrolyte. *ACS Energy Lett.* **2019**, *4* (6), 1427–1431. https://doi.org/10.1021/acsenergylett.9b00975.

(6) Oener, S. Z.; Ardo, S.; Boettcher, S. W. Ionic Processes in Water Electrolysis: The Role of Ion-Selective Membranes. *ACS Energy Lett.* **2017**, *2* (11), 2625–2634. https://doi.org/10.1021/acsenergylett.7b00764.

(7) Patru, A.; Binninger, T.; Pribyl, B.; Schmidt, T. J. Design Principles of Bipolar Electrochemical Co-Electrolysis Cells for Efficient Reduction of Carbon Dioxide from Gas

Phase at Low Temperature. *J. Electrochem. Soc.* **2019**, *166* (2), F34–F43. https://doi.org/10.1149/2.1221816jes.

(8) Chen, Y.; Wrubel, J. A.; Klein, W. E.; Kabir, S.; Smith, W. A.; Neyerlin, K. C.; Deutsch, T. G. High-Performance Bipolar Membrane Development for Improved Water Dissociation. **2020**. https://doi.org/10.1021/acsapm.0c00653.

(9) Bui, J. C.; Digdaya, I.; Xiang, C.; Bell, A. T.; Weber, A. Z. Understanding Multi-Ion Transport Mechanisms in Bipolar Membranes. *ACS Appl. Mater. Interfaces* **2020**, *12* (47), 52509–52526. https://doi.org/10.1021/acsami.0c12686.

(10) Pärnamäe, R.; Mareev, S.; Nikonenko, V.; Melnikov, S.; Sheldeshov, N.; Zabolotskii, V.; Hamelers, H. V. M.; Tedesco, M. Bipolar Membranes: A Review on Principles, Latest Developments, and Applications. *J. Memb. Sci.* **2021**, *617* (August), 118538. https://doi.org/10.1016/j.memsci.2020.118538.

(11) Lin, M.; Digdaya, I. A.; Xiang, C. Modeling the Electrochemical Behavior and Interfacial Junction Profiles of Bipolar Membranes at Solar Flux Relevant Operating Current Densities. *Sustain. Energy Fuels* **2021**. https://doi.org/10.1039/d1se00201e.

(12) Vermaas, D. A.; Wiegman, S.; Smith, W. A. Ion Transport Mechanisms in Bipolar Membranes for (Photo)Electrochemical Water Splitting. *Sustain. Energy Fuels* **2018**, No. 9, 2006–2015. https://doi.org/10.1039/c8se00118a.

(13) McDonald, M. B.; Bruce, J. P.; McEleney, K.; Freund, M. S. Reduced Graphene Oxide Bipolar Membranes for Integrated Solar Water Splitting in Optimal pH. *ChemSusChem* **2015**, *8* (16), 2645–2654. https://doi.org/10.1002/cssc.201500538.

(14) Mcdonald, M. B.; Ardo, S.; Lewis, N. S.; Freund, M. S. Use of Bipolar Membranes for Maintaining Steady-State pH Gradients in Membrane-Supported, Solar-Driven Water Splitting. *ChemSusChem* **2014**, No. 7, 3021–3027. https://doi.org/10.1002/cssc.201402288.

(15) McDonald, M. B.; Freund, M. S.; Hammond, P. T. Catalytic, Conductive Bipolar Membrane Interfaces through Layer-by-Layer Deposition for the Design of Membrane-Integrated Artificial Photosynthesis Systems. *ChemSusChem* **2017**, *10* (22), 4599–4609. https://doi.org/10.1002/cssc.201701397.

(16) McDonald, M. B.; Freund, M. S. Graphene Oxide as a Water Dissociation Catalyst in the Bipolar Membrane Interfacial Layer. *ACS Appl. Mater. Interfaces* **2014**, *6* (16), 13790–13797. https://doi.org/10.1021/am503242v.

(17) Digdaya, I. A.; Sullivan, I.; Lin, M.; Han, L.; Cheng, W. H.; Atwater, H. A.; Xiang, C. A Direct Coupled Electrochemical System for Capture and Conversion of CO_2 from Oceanwater. *Nat. Commun.* **2020**, *11* (1), 1–10. https://doi.org/10.1038/s41467-020-18232-y.

(18) Oener, S. Z.; Twight, L. P.; Lindquist, G. A.; Boettcher, S. W. Thin Cation-Exchange Layers Enable High- Current-Density Bipolar Membrane Electrolyzers via Improved Water Transport. **2021**, 0–7. https://doi.org/10.1021/acsenergylett.0c02078.

(19) Oener, S. Z.; Foster, M. J.; Boettcher, S. W. Accelerating Water Dissociation in Bipolar Membranes and for Electrocatalysis. *Science.* **2020**, eaaz1487. https://doi.org/10.1126/science.aaz1487.

(20) Shen, C.; Wycisk, R.; Pintauro, P. N. High Performance Electrospun Bipolar Membrane with a 3D Junction. *Energy Environ. Sci.* **2017**, *10* (6), 1435–1442.

https://doi.org/10.1039/c7ee00345e.

(21) Craig, N. P. Electrochemical Behavior of Bipolar Membranes. **2013**.

(22) Mareev, S. A.; Evdochenko, E.; Wessling, M.; Kozaderova, O. A.; Niftaliev, S. I.; Pismenskaya, N. D.; Nikonenko, V. V. A Comprehensive Mathematical Model of Water Splitting in Bipolar Membranes: Impact of the Spatial Distribution of Fixed Charges and Catalyst at Bipolar Junction. *J. Memb. Sci.* **2020**, *603*, 118010. https://doi.org/10.1016/j.memsci.2020.118010.

(23) Bui, J. C.; Digdaya, I.; Xiang, C.; Bell, A. T.; Weber, A. Z. Understanding Multi-Ion Transport Mechanisms in Bipolar Membranes. *ACS Appl. Mater. Interfaces* **2020**, acsami.0c12686. https://doi.org/10.1021/acsami.0c12686.

(24) Ramírez, P.; Rapp, H. J.; Reichle, S.; Strathmann, H.; Mafé, S. Current-Voltage Curves of Bipolar Membranes. *J. Appl. Phys.* **1992**, *72* (1), 259–264. https://doi.org/10.1063/1.352124.

(25) Mafé, S.; Ramírez, P.; Alcaraz, A. Electric Field-Assisted Proton Transfer and Water Dissociation at the Junction of a Fixed-Charge Bipolar Membrane. *Chem. Phys. Lett.* **1998**, *294* (4–5), 406–412. https://doi.org/10.1016/S0009-2614(98)00877-X.

(26) Mafé, S.; Ramirez, P. Electrochemical Characterization of Polymer Ion-Exchange Bipolar Membranes. *Acta Polym.* **1997**, *48* (7), 234–250. https://doi.org/10.1002/actp.1997.010480702.

(27) Kaiser, V.; Bramwell, S. T.; Holdsworth, P. C. W.; Moessner, R. Onsager's Wien Effect on a Lattice. *Nat. Mater.* **2013**, *12* (11), 1033–1037. https://doi.org/10.1038/nmat3729.

(28) Onsager, L.; Fuoss, R. M. Irreversible Processes in Electrolytes. Diffusion, Conductance, and Viscous Flow in Arbitrary Mixtures of Strong Electrolytes. *J. Phys. Chem.* **1932**, *36* (11), 2689–2778. https://doi.org/10.1021/j150341a001.

(29) Kaiser, V. The Wien Effect in Electric and Magnetic Coulomb Systems - from Electrolytes to Spin Ice. **2015**, 191.

(30) Onsager, L. Deviations from Ohm's Law in Weak. *J. Chem. Phys.* **1934**, *2* (May 1934), 599–615.

(31) Simons, R. Strong Electric Field Effects on Proton Transfer between Membrane-Bound Amines and Water. *Nature* **1979**, *280* (5725), 824–826. https://doi.org/10.1038/280824a0.

(32) Yan, Z.; Zhu, L.; Li, Y. C.; Wycisk, R. J.; Pintauro, P. N.; Hickner, M. A.; Mallouk, T. E. The Balance of Electric Field and Interfacial Catalysis in Promoting Water Dissociation in Bipolar Membranes. *Energy Environ. Sci.* **2018**, *11* (8), 2235–2245. https://doi.org/10.1039/c8ee01192c.

(33) Grew, K. N.; McClure, J. P.; Chu, D.; Kohl, P. A.; Ahlfield, J. M. Understanding Transport at the Acid-Alkaline Interface of Bipolar Membranes. *J. Electrochem. Soc.* **2016**, *163* (14), F1572–F1587. https://doi.org/10.1149/2.0941614jes.

(34) Wrubel, J. A.; Chen, Y.; Ma, Z.; Deutsch, T. G. Modeling Water Electrolysis in Bipolar Membranes. *J. Electrochem. Soc.* **2020**, *167* (11), 114502. https://doi.org/10.1149/1945-7111/ab9ccb.

(35) Fumatech. Technical Data Sheet for Fumasep FBM. 2020.

(36) Sze, A.; Erickson, D.; Ren, L.; Li, D. Zeta-Potential Measurement Using the Smoluchowski

Equation and the Slope of the Current-Time Relationship in Electroosmotic Flow. *J. Colloid Interface Sci.* **2003**, *261* (2), 402–410. https://doi.org/10.1016/S0021-9797(03)00142-5.

(37) Shen, X. *Molecularly Imprinted Photocatalysts*; Elsevier Inc., 2016. https://doi.org/10.1016/B978-0-12-801301-4.00010-4.

(38) Grew, K. N.; Chiu, W. K. S. A Dusty Fluid Model for Predicting Hydroxyl Anion Conductivity in Alkaline Anion Exchange Membranes. *J. Electrochem. Soc.* **2010**, *157* (3), B327. https://doi.org/10.1149/1.3273200.

(39) Grew, K. N.; Ren, X.; Chu, D. Effects of Temperature and Carbon Dioxide on Anion Exchange Membrane Conductivity. *Electrochem. Solid-State Lett.* **2011**, *14* (12), 5–10. https://doi.org/10.1149/2.011112esl.

(40) Weng, L. C.; Bell, A. T.; Weber, A. Z. Towards Membrane-Electrode Assembly Systems for CO_2 Reduction: A Modeling Study. *Energy Environ. Sci.* **2019**, *12* (6), 1950–1968. https://doi.org/10.1039/c9ee00909d.

(41) Blommaert, M. A.; Verdonk, J. A. H.; Blommaert, H. C. B.; Smith, W. A.; Vermaas, D. A. Reduced Ion Crossover in Bipolar Membrane Electrolysis via Increased Current Density, Molecular Size and Valence. *ACS Appl. Energy Mater.* **2020**, *Just Accep*. https://doi.org/10.1021/acsaem.0c00687.

(42) Kusoglu, A.; Weber, A. Z. New Insights into Perfluorinated Sulfonic-Acid Ionomers. *Chem. Rev.* **2017**, *117* (3), 987–1104. https://doi.org/10.1021/acs.chemrev.6b00159.

(43) Ozmaian, M.; Naghdabadi, R. Modeling and Simulation of the Water Gradient within a Nafion Membrane. *Phys. Chem. Chem. Phys.* **2014**, *16* (7), 3173–3186.

https://doi.org/10.1039/c3cp54015d.

(44) Crothers, A. R.; Darling, R. M.; Kusoglu, A.; Radke, C. J.; Weber, A. Z. Theory of Multicomponent Phenomena in Cation-Exchange Membranes: Part I. Thermodynamic Model and Validation. *J. Electrochem. Soc.* **2020**, *167* (1), 013547. https://doi.org/10.1149/1945-7111/ab6723.

(45) U.S. Geological Survey. PHREEQC (Version 3) - A Computer Program for Speciation, Batch-Reaction, One-Dimensional Transport, and Inverse Geochemical Calculations.

(46) Zumdahl, S.; DeCoste, D. *Chemical Principles*, 8th ed.; Cengage Learning: Boston, MA, 2016.

(47) Eigen, M. Proton Transfer, Acid-Base Catalysis, and Enzymatic Hydrolysis. *Angew. Chemie* **1964**, *3* (I), 1–19.

(48) Okada, T.; Satou, H.; Okuno, M.; Yuasa, M. Ion and Water Transport Characteristics of Perfluorosulfonated Ionomer Membranes with H^+ and Alkali Metal Cations. *J. Phys. Chem. B* **2002**, *106* (6), 1267–1273. https://doi.org/10.1021/jp013195l.

(49) Crothers, A. R.; Darling, R. M.; Kusoglu, A.; Radke, C. J.; Weber, A. Z. Theory of Multicomponent Phenomena in Cation-Exchange Membranes: Part II. Transport Model and Validation. *J. Electrochem. Soc.* **2020**, *167* (1), 013548. https://doi.org/10.1149/1945-7111/ab6724.

(50) Peng, J.; Zawodzinski, T. A. Ion Transport in Phase-Separated Single Ion Conductors. *J. Memb. Sci.* **2018**, *555* (January), 38–44. https://doi.org/10.1016/j.memsci.2018.03.029.

(51) Kamcev, J.; Paul, D. R.; Manning, G. S.; Freeman, B. D. Ion Diffusion Coefficients in Ion

Exchange Membranes: Significance of Counterion Condensation. *Macromolecules* **2018**, *51* (15), 5519–5529. https://doi.org/10.1021/acs.macromol.8b00645.

(52) Kamcev, J.; Galizia, M.; Benedetti, F. M.; Jang, E. S.; Paul, D. R.; Freeman, B. D.; Manning, G. S. Partitioning of Mobile Ions between Ion Exchange Polymers and Aqueous Salt Solutions: Importance of Counter-Ion Condensation. *Phys. Chem. Chem. Phys.* **2016**, *18* (8), 6021–6031. https://doi.org/10.1039/c5cp06747b.

(53) Natzle, W. C.; Moore, C. B. Recombination of Hydrogen Ion (H^+) and Hydroxide in Pure Liquid Water. *J. Phys. Chem.* **1985**, *89* (12), 2605–2612. https://doi.org/10.1021/j100258a035.

(54) Critchfield, F. E.; Gibson, J. A.; Hall, J. L. Dielectric Constant for the Dioxane-Water System from 20 to 35°. *J. Am. Chem. Soc.* **1953**, *75* (8), 1991–1992. https://doi.org/10.1021/ja01104a506.

(55) Danilovic, N.; Subbaraman, R.; Strmcnik, D.; Chang, K. C.; Paulikas, A. P.; Stamenkovic, V. R.; Markovic, N. M. Enhancing the Alkaline Hydrogen Evolution Reaction Activity through the Bifunctionality of $Ni(OH)_2$/Metal Catalysts. *Angew. Chemie - Int. Ed.* **2012**, *51* (50), 12495–12498. https://doi.org/10.1002/anie.201204842.

(56) Subbaraman, R.; Tripkovic, D.; Strmcnik, D.; Chang, K. C.; Uchimura, M.; Paulikas, A. P.; Stamenkovic, V.; Markovic, N. M. Enhancing Hydrogen Evolution Activity in Water Splitting by Tailoring Li^+-$Ni(OH)_2$-Pt Interfaces. *Science.* **2011**, *334* (December), 1256–1260.

(57) Zhang, T.; Li, Z.; Zhang, J.; Wu, J. Enhance CO_2-to-C_{2+} Products Yield through Spatial Management of CO Transport in Cu / ZnO Tandem Electrodes. *J. Catal.* **2020**, *387*, 163–

169. https://doi.org/10.1016/j.jcat.2020.05.002.

(58) Chen, C.; Li, Y.; Yu, S.; Louisia, S.; Jin, J.; Li, M.; Ross, M. B.; Yang, P. Cu-Ag Tandem Catalysts for High-Rate CO_2 Electrolysis toward Multicarbons. *Joule* **2020**, *4* (8), 1688–1699. https://doi.org/10.1016/j.joule.2020.07.009.

(59) Wang, L.; Higgins, D. C.; Ji, Y.; Morales-Guio, C. G.; Chan, K.; Hahn, C.; Jaramillo, T. F. Selective Reduction of CO to Acetaldehyde with CuAg Electrocatalysts. *Proc. Natl. Acad. Sci. U. S. A.* **2020**, *117* (23), 12572–12575. https://doi.org/10.1073/pnas.1821683117.

(60) Strathmann, H.; Krol, J. J.; Rapp, H. J.; Eigenberger, G. Limiting Current Density and Water Dissociation in Bipolar Membranes. *J. Memb. Sci.* **1997**, *125* (1), 123–142. https://doi.org/10.1016/S0376-7388(96)00185-8.

(61) Krol, J. J.; Jansink, M.; Wessling, M.; Strathmann, H. Behaviour of Bipolar Membranes at High Current Density Water Diffusion Limitation. *Sep. Purif. Technol.* **1998**, *14* (1–3), 41–52. https://doi.org/10.1016/S1383-5866(98)00058-6.

(62) Foley, G. *Encyclopedia of Membranes*; 2016. https://doi.org/10.1007/978-3-662-44324-8.

(63) Ridley, M. K.; Hackley, V. A.; Machesky, M. L. Characterization and Surface-Reactivity of Nanocrystalline Anatase in Aqueous Solutions. *Langmuir* **2006**, *22* (26), 10972–10982. https://doi.org/10.1021/la061774h.

(64) Liu, X.; Cheng, J.; Lu, X.; Wang, R. Surface Acidity of Quartz: Understanding the Crystallographic Control. *Phys. Chem. Chem. Phys.* **2014**, *16* (48), 26909–26916. https://doi.org/10.1039/c4cp02955k.

For Table of Contents Only (TOC Graphic)